Spin-polarized sextuple excitations in ferromagnetic materials

Lei Jin, Ying Liu,* Wei-Wang Yu, Xiaoming Zhang, Guodong Liu, and Xuefang Dai†
State Key Laboratory of Reliability and Intelligence of Electrical Equipment, Hebei University of Technology, Tianjin 300130, China and School of Materials Science and Engineering, Hebei University of Technology, Tianjin 300130, China

(Received 24 August 2021; accepted 13 June 2022; published 27 June 2022)

The most fundamental symmetry in condensed matter physics is the crystallographic symmetry, such that solids could exhibit unconventional excitations beyond Dirac and Weyl fermions. Among the unconventional fermions, the sextuple excitation has been predicted in many nonmagnetic materials. However, the study of magnetic sextuple excitations has fallen behind because of the complicated magnetic structures of materials. Here we perform a systematic search for ferromagnetic (FM) sextuple points (SPs) in the absence of spin-orbit coupling. Based on 230 space groups (SGs), we find there are 5 SGs that could host SPs at high-symmetry points. Regarding the stability of the sextuple excitation, we reveal that the minimum little point group at where the SP locates is T_d. To support this result, we construct the effective model based on the $k \cdot p$ method, from which the linear dispersion can be read off. Via first-principles calculations, we also identify 67 FM material candidates, which realize the SPs with completely/incompletely spin polarized. To support our theory, we pick one of the FM materials, Rb_4O_6, as an example in which there is a fully spin-polarized SP. Finally, our work paves the way to study the spin-polarized SPs and provides a platform to realize the spintronic associated with sextuple excitations.

DOI: 10.1103/PhysRevB.105.245141

I. INTRODUCTION

The fundamental symmetry, Poincaré symmetry, in high-energy physics exerts strict constraints on fermions of which only three types of fermions exist [1], i.e., Weyl, Dirac, and Majorana fermions. Recently, their counterparts in low-energy physics have been actively realized in condensed matter [2–7]. These massless Dirac/Weyl fermions exhibit fourfold/twofold degeneracy and linear dispersion along all directions. However, the elementary symmetry in solids is the crystallographic symmetry, which puts a relaxed constraint on quasiparticles in solids. Therefore beyond Dirac/Weyl fermions, the crystallographic symmetry allows the extension of the concept of fermions in solids.

With this generalization, the linearity of dispersion for particles is not necessarily required by the crystallographic symmetry such that high-order Weyl/Dirac fermions could be stabilized by symmetry in solids [8–13]. Besides the fermions with twofold/fourfold degeneracy, the crystallographic symmetry allows the fermions in richer types compared with Poincaré symmetry in high-energy physics [14], i.e., triple degenerate point [15–18], sextuple point (SP) [19–29], and octuple point [30]. These unconventional fermions have also been found to have novel physical properties. For example, Wang *et al.* theoretically verified that materials with long Fermi arcs have high catalytic performance [31]. Double Weyl fermions (high-order Weyl fermions) may have non-Fermi liquid interaction effects and anisotropic thermoelectric properties [32–36]. Multifold fermions may induce a circular photogalvanic effect with a large quantized value, because their topological charges are several times that of conventional Weyl fermions [25,29,37]. Notably, the SP, as unconventional fermions, also attracted tremendous interest. Meng *et al.* proposed that sixfold- and fourfold-degenerate points are identified as the underlying reason of the enhanced catalytic ability in $C_{12}A_7{:}4e^-$-based catalysts [38]. Therefore their novel physical properties are also worth exploring. However, few candidate materials with sextuple fermions have been found so far; thus it is urgent to find more candidate materials. Remarkably, Yu *et al.* performed a schematic research of the emergent fermions in solids based on 230 space groups (SGs) [39]. Notably, the SP was predicted and attracted tremendous interest. It has been predicted to exist in electride $Li_{12}Mg_3Si_4$ [19], $PtBi_2$ [28], $PdSb_2$ [22,23,40], and other materials. In particular, the SP has been experimentally observed in $PdSb_2$ [22,23,40]. So far, most studies about the SP is limited to nonmagnetic (NM) systems; magnetic SP has not yet been discovered due to the complex magnetic structure of magnetic materials.

It is well known that magnetic order will break time-reversal symmetry, making the protection of SPs challenging. Therefore so far, there is no work regarding SPs in magnetic materials. However, in the application perspective, it is much desirable to discovery the magnetic SP, especially those in a single spin channel around the Fermi level, i.e., to realize a half-metal state with the fully spin-polarized SP. As a consequence, the physical properties associated with SPs only happen in one single channel. Furthermore, the spin polarization is convertible by controlling the magnetization. Thus

*ying_liu@hebut.edu.cn
†xuefangdai@126.com

TABLE I. List of SGs hosting SPs. The point group is abbreviated to PG.

SG	BZ	Position	PG	IRRs
218	Γ_c	R	T_d	$\{R_9 \oplus R_{10}\}$
220	Γ_c^v	H		
222, 223	Γ_c	R	O_h	R_{14}
230	Γ_c^v	H		

it has a great potential in spintronic devices, possessing the advantages of high speed and low-energy consumption.

In this work, we perform a schematic work for identifying spin-polarized SPs in ferromagnetic (FM) systems. We need to point out that since spin-down and spin-up channels in a FM system are separated, if we focus on one spin channel, it will seem like a spinless case. Therefore to achieve this aim, we search all single-valued 230 SGs, unveiling 5 SGs that could host the SPs at high-symmetry points. We summarize the results in Table I, and our key findings are (i) the minimum point group at positions where the SPs locate is T_d. The SP is a crossing between two three-dimensional (3D) irreducible representations (IRRs). (ii) The SP can be regarded as a composition of two spin-1 fermions with opposite chirality, resulting in a net Chern number. Furthermore, we present the $k \cdot p$ model to characterize the physical features in low energy, from which the linearity of dispersion can be read off. Based on the symmetry, via first-principles calculations, we identify the possible material candidates. Finally, we discover 67 FM material candidates which could host SPs in a metal state, providing a fruitful platform for spin-polarized SPs. In our main text, we pick up FM material Rb_4O_6 to study the SP, including the electronic band structure and surface states, which agree well with our symmetry analysis.

Before going into detailed analysis, it is necessary to emphasize that as far as we know, our work is the *first* work to study the fully spin-polarized SPs in a half-metal state. It not only provides a platform to study the FM SPs but also provides a guideline to find the SPs in spinless systems, like the phononic SPs.

II. SYMMETRY ANALYSIS

Without loss of generality, we could chose the magnetization direction to be along the z direction. In FM state, the spin-up and spin-down channels decouple in the absence of spin–orbit coupling (SOC), which could lead to a half-metal state. Only focusing on one spin channel, it resembles a spinless system. The band crossings in the electronic band structure is therefore determined by the single-valued SGs. Based on this, we search over all IRRs at high-symmetry point of 230 SGs, finding 5 SGs that could host SPs (see in Table I). The SPs could correspond to a band crossing between two 3D IRRs or a 6D IRR.

To characterize the features of SPs, we construct the effective model in the basis which belongs to these IRRs. Since the symmetry exerts constraints on the effective model, they satisfy that

$$\mathcal{D}(R)\mathcal{H}(R^{-1}\boldsymbol{k})\mathcal{D}^{-1}(R) = \mathcal{H}(\boldsymbol{k}), \tag{1}$$

with R running over all of the generating elements at SP and $\mathcal{D}(R)$ the matrix representation of corresponding symmetry. Here $\boldsymbol{k}$ is measured from the SP.

In the following, we discuss the symmetry that enforces the SPs. We summarize the main result in Table I.

By searching over all of single-valued IRRs, we find that the minimum point group at the high-symmetry points that protecting the SPs is T_d, and it is the subgroup of O_h. Point group T_d is generated by any S_{4i} (with $i = x, y, z$) and $C_{3,111}$. Here we choose S_{4x}; S_{4x} is the rotation reflection generated by the fourfold rotation along the x direction and inversion symmetry. $C_{3,111}$ is a threefold rotation along the [111] direction. There are two 3D IRRs listed in Table I, in which the generating elements could take the following forms:

$$\begin{aligned} S_{4x} &= iW \oplus (-iW),\ W = \begin{bmatrix} 0 & 1 & 0 \\ -1 & 0 & 0 \\ 0 & 0 & -1 \end{bmatrix}, \\ C_{3,111} &= A \oplus A,\ A = \begin{bmatrix} 0 & 0 & 1 \\ 1 & 0 & 0 \\ 0 & 1 & 0 \end{bmatrix}, \\ \mathcal{T} &= \sigma_x \otimes (I_{3\times 3}\mathcal{K}). \end{aligned} \tag{2}$$

Here $\mathcal{K}$ is the complex conjugation; $I_{3\times 3}$ refers to a 3×3 identity matrix. An effective model could be derived based on relationships in Eqs. (1) and (2) expressed in the following forms,

$$\begin{aligned} \mathcal{H}_{T_d}^{SP}(\boldsymbol{k}) = {} & c\sigma_z \otimes (k_x\lambda_1 + k_y\lambda_4 + k_z\lambda_6) \\ & + i\alpha(\cos\phi\sigma_x + \sin\phi\sigma_y) \otimes (k_x\lambda_2 - k_y\lambda_5 + k_z\lambda_7); \end{aligned} \tag{3}$$

λ's are the 3×3 Gell-Mann matrices, σ's are the Pauli matrices, and ϕ is an angle. Here c is real parameters; α is imaginary. Interestingly, we find that this effective model includes chiral and antichial terms, most specially,

$$h_C(\boldsymbol{k}) = k_x\lambda_2 - k_y\lambda_5 + k_z\lambda_7 \tag{4}$$

$$h_{\text{anti}-C}(\boldsymbol{k}) = k_x\lambda_1 + k_y\lambda_4 + k_z\lambda_6. \tag{5}$$

For the chiral term, it could be rewritten as $h_C(\boldsymbol{k}) = \boldsymbol{k} \cdot \boldsymbol{S}$, where $\boldsymbol{S}$ is the spin-1 matrices, with $S_x = \lambda_1,\ S_y = \lambda_4,\ S_z = \lambda_6$.

The point group O_h can be derived from T_d by adding the inversion symmetry, whose generators can be chosen as $S_6 = PC_{3,111}$ and S_{4x}. As a consequence, the antichiral term vanishes, and the Hamiltonian is given by

$$\mathcal{H}_{O_h}^{SP}(\boldsymbol{k}) = i\alpha(\cos\phi\sigma_x + \sin\phi\sigma_y) \otimes h_C(\boldsymbol{k}). \tag{6}$$

Particularly, when $\phi = \pi/2$ and $|\alpha| \gg |c|$, the effective Hamiltonians belonging to two PGs are identical, taking the following form,

$$\mathcal{H}^{SP}(\boldsymbol{k}) = \begin{bmatrix} 0 & \alpha(\boldsymbol{k}\cdot\boldsymbol{S}) \\ -\alpha(\boldsymbol{k}\cdot\boldsymbol{S}) & 0 \end{bmatrix}, \tag{7}$$

suggesting two spin-1 fermions of opposite chirality. These two spin-1 fermions are degenerate at the same point enforced by $\mathcal{T}$; thus a SP with zero Chern number appears.

III. MATERIAL REALIZATION

According to the symmetry, we have identified 67 FM materials that are potential SP metals. All the materials screened are summarized in Table II, classified by SPs. In Table II, we not only give the positions of the SPs in the Brillouin zone (BZ), the lattice parameters of the materials, the spin polarization ratio (SPR; many of which have 100% SPR), the difference between the energy of the NM/AFM states and the FM states, but also give the energy positions of SP. Some of these materials have been experimentally confirmed to be ferromagnetic materials [41–56]. The SPR is defined as $(N_{up} - N_{dn})/(N_{up} + N_{dn})$, where N_{up} and N_{dn} are used to represent the density of state (DOS) of spin-up and spin-down electrons at the Fermi level, respectively. When SPR = 0, the materials belong to NM materials or insulators; when SPR $\leqslant$ 1, the materials belong to the magnetic material; especially when SPR =1, the system has 100% spin polarization and the material belongs to half-metal. In this paper, we chose Rb_4O_6 as an example to support our theory.

In this work, we use the Vienna ab initio Simulation Package (VASP)[57] for the first-principles calculations. The VASP is used the projector augmented wave (PAW) method in the framework of density-functional theory (DFT)[58]. For the exchange correlation potential, we use the generalized gradient approximation of the Perdew-Burke-Ernzerhof functional [59]. The cutoff energy is set as 500 eV. A Γ-centered k mesh of 11×11×11 is used for the BZ sampling. The topological features of surface states are calculated based on the maximally localized Wannier functions [60,61] realized by using the WANNIERTOOLS package [62].

A. Crystal structure and magnetic properties

Material Rb_4O_6 has a cubic crystal structure belonging to SG $Ia3d$ (No. 220). As shown in Fig. 1(a), one Rb atom bonds with six O atoms. Within a unit cell, Rb and O atoms occupy the 16c (−0.0545, −0.0545, −0.0545) and 24d (−0.447, 0, −0.25) Wyckoff sites, respectively. Figure 1(b) shows the primitive cell of Rb_4O_6 with 8 Rb and 12 O atoms. The fully relaxed lattice constants are $a = b = c = 9.383$ Å, which match well with the experimental values ($a = b = c = 9.324$Å [63]). In our calculations, we adopt the optimized lattice structures. The Rb_4O_6 has an unconventional stoichiometry, which may introduce magnetism. We investigate the NM, FM, and antiferromagnetic (AFM) states in the Rb_4O_6 compound. The results show that the FM state is 0.565 and 0.264 eV lower than the NM and AFM, respectively, confirming that the Rb_4O_6 compound has the FM ground state. We also consider three magnetization directions with the highest potential, including [1 0 0], [1 1 0], and [1 1 1]. The results show that the easy magnetic axis is [1 1 1]. In the FM state, the magnetic anisotropy energies (MAE $= E_{[100] \text{ or } [110]} - E_{[111]}$) of the other two directions [1 0 0] and [1 1 0] are 38 and 2 meV, respectively. The total magnetic moment is 4 μB per primitive cell and is mostly contributed to by the light element (oxygen) atom, as shown in Fig. 1(d). The fundamental mechanisms of magnetism in the Rb_4O_6 have been well clarified by Attema *et al.* [64]. It contains two superoxide anions and one peroxide anion in a cubic lattice; the chemical formula can be written as $(Rb^+)_4(O_2^-)_2(O_2^{2-})$. The detailed information has been studied by elastic and inelastic neutron diffraction [63]. The superoxide (also known as hyperoxide) anion (O_2^-) is magnetic since it contains one unpaired electron in the π^* antibonding level, while the filled π^* level in the peroxide anion (O_2^{2-}) renders it nonmagnetic. They are stabilized by alkali metal cations (Rb^+) to form ionic salts; this type of material is more likely to possess strong magnetic exchange interactions and exhibit long-range-ordering phenomena than molecule-based systems due to the close proximity of magnetic species in the ionic lattice.

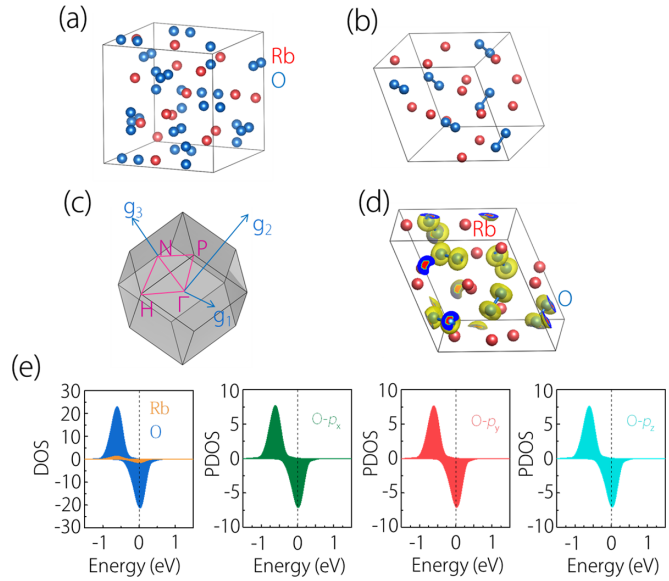

FIG. 1. (a) Unit cell and (b) primitive cell structure for Rb_4O_6. (c) The bulk BZ for Rb_4O_6. (d) The spin density of Rb_4O_6. The magnetic moment comes from O. (e) The total density of state (DOS) and the projected density of state (PDOS).

B. Band structure in the absence of SOC

After determining the magnetic structure, we then study the electronic band structure via DFT calculation. From Fig. 1(e), one can observe that the bands around the Fermi level are mainly contributed by p orbitals from the O atom. Figures 2(a) and 2(b) show the spin-resolved band structures for the Rb_4O_6 compound without considering SOC. One observes that band structures in the spin-up and spin-down channels show distinct conducting behaviors. Comparing Figs. 2(a) and 2(b), one clearly sees that the spin-up bands have a large band gap of 3.524 eV around the Fermi level, while the spin-down bands definitely exhibit a metallic character. Hence the low-energy states are fully spin-polarized in the spin-down channel, leading to a half-metal.

Focusing on band structure of the spin-down channel, there are several band crossings around the Fermi level, including a SP at the H point, a quadratic contact triple point (TP) at the Γ point, and a Dirac point (DP) at the P point. Our calculation results are consistent with the prediction proposed by Yu *et al.* [39]. Most importantly, these multifold-degenerate points are very close to the Fermi level without other extraneous bands. The SP of Rb_4O_6 is locating at −0.059 eV, which is much

TABLE II. List of materials candidates hosting SPs. We list the SGs, the location of SP, lattice constant, the SPR, ΔE_1 (in units of eV), ΔE_2 (in units of eV), and the energy positions of SP (in units of eV). Here ΔE_1 and ΔE_2 represent the difference between the energy of the NM/AFM states and the FM states, respectively. Note that ΔE_2 of $Nd_5Mo_3O_{16}$ represents the difference between the energy of the ferrimagnetic and FM states, and there is no AFM state.

SG	Location	Compound	Lattice (Å)	SPR	ΔE_1	ΔE_2	SP
218	R	Li_7CrN_4	9.627	100%	1.264	0.170	−0.017
		Li_7NiN_4	9.622	100%	0.054	0.026	−0.277
		Li_7ReN_4	9.844	100%	1.247	0.354	−0.284
220	H	Eu_4As_3[41]	9.186	100%	39.515	0.197	−0.059
		Ce_4As_3	8.903	44.4%	0.269	0.192	0.046
		Ce_4Bi_3[42]	9.714	95.2%	0.902	0.528	−0.074
		Ce_4Sb_3[43]	9.442	48%	0.458	0.215	0.012
		Gd_4Sb_3[44]	9.345	100%	33.562	0.309	0.107
		Nd_4Bi_3	9.696	100%	11.316	0.637	−0.130
		Pr_4Bi_3	9.775	100%	5.388	0.767	−0.096
		Pr_4Sb_3	9.581	100%	4.946	0.561	−0.117
		Tb_4Bi_3[44]	9.436	23.3%	6.7×10^{-5}	7.9×10^{-5}	−0.137
		Ce_3S_4[45]	8.537	97.2%	0.435	0.312	0.059
		Ce_3Se_4[46]	8.912	99.3%	0.599	0.330	0.050
		Ce_3Te_4	9.542	99.4%	0.734	0.269	0.004
		Cr_3N_4	6.803	38.9%	0.753	0.639	0.313
		Eu_3S_4[47]	8.598	100%	46.583	1.160	−0.230
		Gd_3S_4[48]	8.419	86.5%	54.268	0.013	0.240
		Gd_3Se_4[48]	8.762	84.9%	53.500	0.034	0.220
		Np_3Se_4	8.401	99.4%	6.131	0.510	−0.016
		Np_3Te_4	9.321	100%	9.459	0.645	−0.020
		Np_3As_4[49]	8.498	96.2%	5.003	0.277	0.035
		Pa_3Sb_4	9.172	77.5%	0.075	0.076	−0.012
		U_3As_4[50]	8.498	99.2%	1.528	0.694	−0.132
		U_3Bi_4[51]	9.361	66.6%	2.645	0.095	−0.155
		U_3Sb_4[51]	9.102	100%	2.104	0.331	−0.116
		U_3Se_4[52]	8.671	90.1%	2.115	0.267	0.033
		U_3Te_4[52]	9.282	98.1%	3.209	0.394	0.021
		U_3P_4[50]	8.177	81.3%	0.709	0.416	−0.093
		Np_2C_3[53]	8.027	67.7%	12.051	0.012	0.013
		U_2C_3	8.050	36.6%	0.452	0.229	−0.114
		Rb_4O_6	9.383	100%	0.565	0.264	−0.059
		$Ce_3Bi_4Au_3$	10.340	97.7%	0.473	0.473	−0.028
		$Ce_3Bi_4Pd_3$	10.083	84%	0.058	0.047	0.020
		$Ce_3Cu_3Sb_4$[54]	9.727	95.9%	0.327	0.327	−0.022
		$Th_3Co_3Sb_4$[55]	9.605	100%	0.371	0.260	−0.092
		$U_3Sb_4Pd_3$	9.734	100%	2.439	2.339	−0.026
		$U_3Co_3Sb_4$[56]	9.318	100%	0.958	0.957	0.003
		$U_3Sb_4Pt_3$	9.760	100%	2.218	2.120	−0.039
		$U_3Sn_4Au_3$	9.910	51%	1.864	1.863	−0.018
		$U_3Sn_4Pt_3$	9.753	41.5%	0.614	0.510	−0.067
222	R	$Nd_5Mo_3O_{16}$	11.138	100%	13.554	15.929	0.011
223	R	AlV_3	4.809	15.7%	0.017	0.017	0.070
		FeH_3	3.285	11.5%	0.245	0.001	1.405
		PaH_3	6.641	55.3%	0.054	0.054	0.138
		UH_3	4.126	70.6%	0.695	0.335	0.040
		VGe_3	5.098	13.7%	0.426	0.416	0.180
		Nb_3Au	5.256	42%	0.027	0.027	0.547
		V_3Au	4.881	37.1%	0.032	0.017	0.221
		V_3Ga	4.790	17.3%	0.017	0.017	0.060
		V_3Pt	4.815	27.8%	3.19×10^{-4}	5.46×10^{-4}	0.609
		V_3Si	4.702	39.3%	0.004	0.004	−0.070
		V_3Sn	4.965	43.8%	1.77×10^{-4}	1.85×10^{-4}	0.008

TABLE II. (*Continued.*)

SG	Location	Compound	Lattice (Å)	SPR	ΔE_1	ΔE_2	SP
230	H	$Li_3Co_2Ge_3O_{12}$	11.862	100%	1.406	0.483	0.018
		$Li_3Fe_2Ge_3O_{12}$	12.131	100%	6.616	0.263	0.027
		$Li_3Ge_3Mo_2O_{12}$	12.377	100%	1.424	0.206	−0.051
		$Li_3Mn_2P_3O_{12}$	11.840	100%	11.901	0.283	−0.024
		$Li_3Ni_2Ge_3O_{12}$	11.851	32.3%	0.068	0.068	−0.158
		$Li_3V_2P_3O_{12}$	11.832	100%	6.771	0.408	0.026
		$Mg_3V_2Si_3O_{12}$	11.834	100%	7.269	0.178	0.037
		$Mn_2Fe_3Si_3O_{12}$	11.898	21.9%	35.070	6.299	0.013
		$Na_3Ge_3Mo_2O_{12}$	12.601	100%	1.279	0.291	−0.023
		$Na_3Co_2Ge_3O_{12}$	12.127	100%	1.363	0.522	−0.029
		$Na_3Fe_2Ge_3O_{12}$	12.404	100%	6.351	0.206	−0.025
		$Na_3Li_3Ti_2F_{12}$	12.650	100%	2.209	0.034	0.011
		$Na_3Mn_2Ge_3O_{12}$	12.269	100%	8.424	0.377	−0.065
		$V_2Fe_3Si_3O_{12}$	11.904	100%	45.628	24.432	0.028

closer to the Fermi level than other materials with SPs, including AlPt (−0.6 eV) [24], $PdSb_2$ (−0.27 eV) [22], and PdBiSe (−0.76 eV) [27], and SPs in these materials have been observed in experiment; thus the SP of Rb_4O_6 is also promising to be observed in experiment. The SP is formed by four electronlike bands and two holelike bands, consistent with the 3D band structure that one observes in Fig. 2(c). The TP and DP are, respectively, located at 0.009 and −0.196 eV, and their 3D band structures are shown in Figs. 2(d) and 2(e). It is well known that the main physical consequence of nontrivial band crossings in the bulk is the appearance of gapless surface states. We therefore plot the surface spectra for Rb_4O_6 on different surfaces [see in Figs. 3(b), 3(e), and 3(h)]. Most specifically, we plot the surface spectra for SP on the (0 1 0) plane, TP on (1 $\bar{1}$ 0) plane, and DP on (0 0 1) plane, respectively. Remarkably, there are Fermi arcs emanating from their projections. In order to see the evolution of the surface states, we then show the constant energy slices for SP at $E = 5.98$ eV [in Fig. 3(c)], TP at $E = -0.002$ eV [in Fig. 3(f)], and DP at $E = -0.24$ eV [in Fig. 3(i)]. We need to point out that the SP point we select is the one at a higher energy in order to clearly exhibit the surface states.

In the topological perspective, the stability of the Fermi arcs is ensured by topology. However, as aforementioned, if the SP looks like two copies of two spin-1 fermions of opposite chirality, a zero Chern number is expected. Indeed, our calculation shows that SP, TP, and DP locate at the invariant

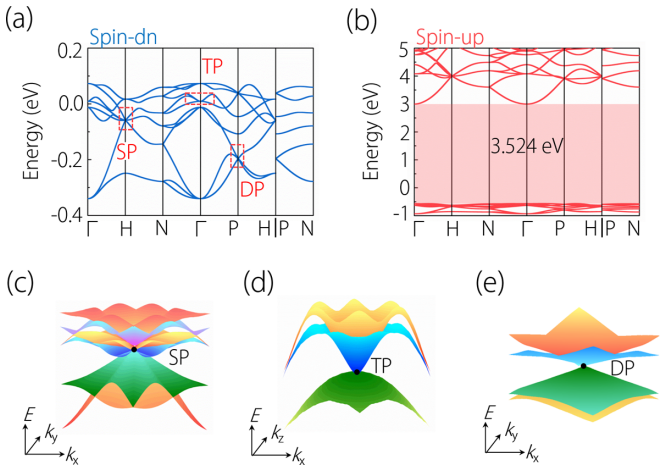

FIG. 2. The electronic band structures of the Rb_4O_6 compound in the absence of SOC. (a) The spin-down band structure, showing metallic character with several bands crossing the Fermi level. The dashed frame regions show the positions of sextuple, triple, and Dirac points, which are labeled as SP, TP, and DP, respectively. (b) The spin-up band structure, exhibiting insulating character with a big band gap of 3.524 eV. (c)–(e) show the three-dimensional plots of band dispersions near SP, TP, and DP.

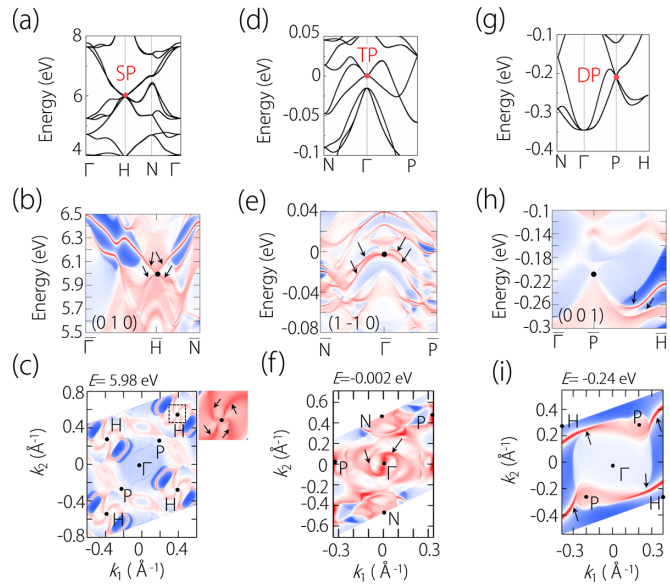

FIG. 3. (a) The band structure around SP. (b) Projected spectrum on the (0 1 0) surface for SP. (c) The corresponding constant energy slice for (b) at $E = 5.98$ eV. (d) The band structure around TP. (e) Projected spectrum on the (1 $\bar{1}$ 0) surface for TP. (f) The corresponding constant energy slice for (e) at $E = -0.002$ eV. (g) The band structure around DP. (h) Projected spectrum on the (0 0 1) surface for DP. (i) The corresponding constant energy slice for (h) at $E = -0.24$ eV. The black dots in (b), (e) and (h) indicate the positions of the SP, TP and DP. Fermi arcs are pointed by arrows.

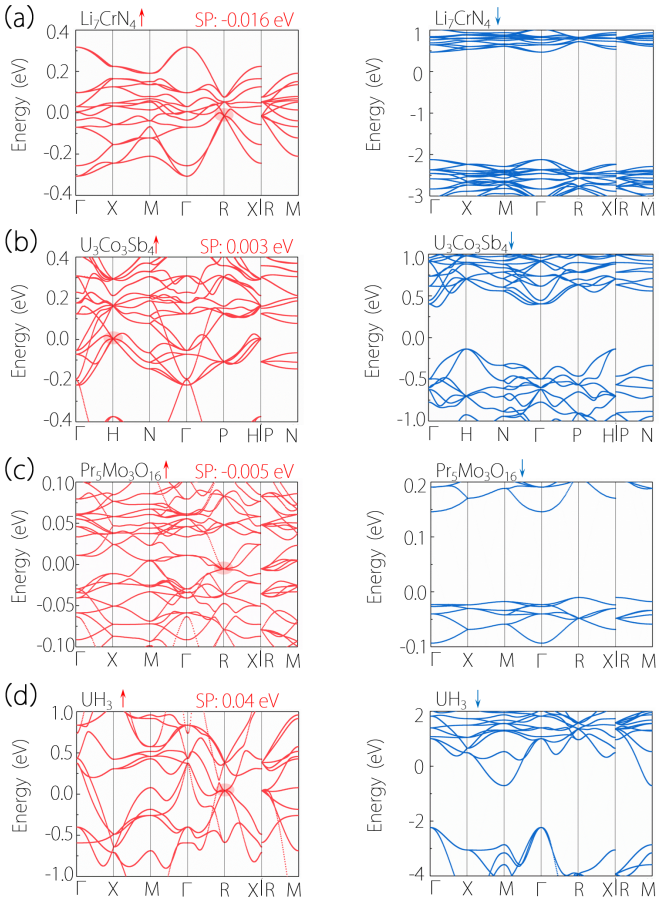

FIG. 4. The electronic band structures of (a) Li_7CrN_4, (b) $U_3Co_3Sb_4$, (c) $Pr_5Mo_3O_{16}$ and (d) UH_3.

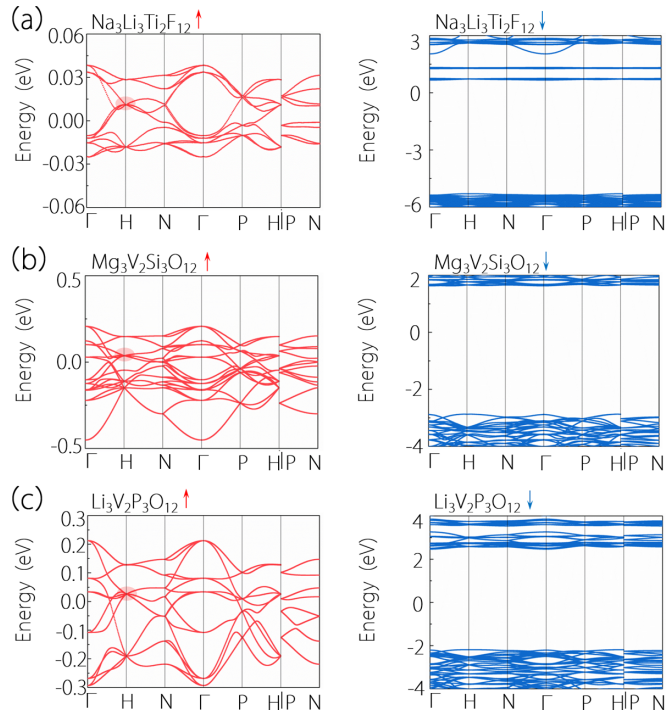

FIG. 5. The electronic band structures of (a) $Na_3Li_3Ti_2F_{12}$, (b) $Mg_3V_2Si_3O_{12}$ and (c) $Li_3V_2P_3O_{12}$.

subspace of $M_{01\bar{1}}$, resulting in a zero Chern number. Thus the Fermi arcs stemming from the band crossing should be trivial. In fact, the nontrivial Fermi arcs have been discussed in Dirac semimetals (i.e., Na_3Bi [65,66] and Cd_3As_2 [67–69]), in which two Fermi arcs emanating from the DP projections do not show topological robustness [70]. Two Fermi arcs starting from DP at the P point indeed exhibit the same result [see Figs. 3(h) and 3(i)]. In fact, such trivial surface states are also expected to emanate from SP and TP, it seems like the case in Dirac semimetals. Therefore it is reasonable that there are Fermi arcs emanating from their projections. Furthermore, on their projected surface, the Fermi arcs are connected by twofold rotation symmetry, e.g., C_{2y} for SP [see in Fig. 3(c)], and $C_{1\bar{1}0}$ for TP [see in Fig. 3(f)]. Finally, we have analyzed that all of the surface states occur in the spin-down channel, suggesting that they are of 100% spin polarization.

As shown in Fig. 4, we also show the band structures of other candidate materials with SPs in Table II. In these candidate materials, the distance from SPs to Fermi level is less than 0.04 eV and even less than 0.005 eV.

IV. DISCUSSION AND CONCLUSION

We have demonstrated that there are five SGs host SP at high-symmetry point, and T_d is the minimum PG to support a SP. Based on the symmetry, when SOC is neglected, we identify 67 FM material candidates, and several of them could achieve a 100% spin polarization, leading to a half-metal state. By taking Rb_4O_6 as an example, we find that there is a fully spin-polarized SP at the H point, and surface states of full spin-polarization stem from its projection. Moreover, the magnetic moment of Rb_4O_6 mainly comes from the light element (oxygen) atom, and it can be seen from the DOS that the bands forming the SP are mainly contributed by the O atom; thus the SP of Rb_4O_6 is very little affected by the SOC effect. The Rb_4O_6 is the material example with negligible SOC effect. In addition, we also show band structures of other materials with relatively weak SOC strength in Fig. 5. The above discussion regarding the fully spin-polarized SP is in the absence of SOC. When SOC is taken into consideration, clearly, the FM term breaks the time-reversal symmetry and certain spatial symmetries. When the magnetic moment is along the [1 0 0] direction, only S_{4x} is still preserved, which could lead to a quadratic Weyl point with broken time-reversal symmetry [71]. On the other hand, only the $C_{3,111}$ remains when the magnetic moment is in the [1 1 1] direction, and such a threefold rotation symmetry could protect a Weyl point with linear dispersion. Moreover, the phase transition can also be realized by applying strain [19].

In conclusion, we schematically search over all possible SPs in 230 SGs at high-symmetry points in the absence of SOC. We reveal that there are 5 SGs (218, 220, 222, 223, 230) hosting the SP and list their positions in Table II. In addition, T_d is the minimum point group which host the SP, and its corresponding effective model is constructed. The main features of SP could be read from its effective model, including the linearity of dispersion, and zero Chern number. Based on the symmetry analysis, we identify 67 FM material candidates and summarize the results in Table II, showing the incomplete

and complete 100% spin-polarized materials with SP. In the main text, we provide an existing material, Rb_4O_6, to study the SP fermions. Via DFT calculation, we demonstrated that it has a FM ground state with 100% spin-polarization. Since the magnetic moment of Rb_4O_6 is from *p* orbitals, states have much weaker localization. As a result, the material is promising for higher carrier mobility and longer spin coherence length. From the band structure, we verify the presence of fully spin-polarized SP; at the same time, there are also some other fermions, i.e., TP and DP. One of the most representative features of the topological nodal point, the Fermi arc, is also clearly shown in their surface spectra. Thereby this work provides a rich data set of sextuple fermions in FM materials, paving the way to study the application in spintronic devices.

ACKNOWLEDGMENTS

This work is supported by the Nature Science Foundation of Hebei Province, the S&T Program of Hebei (Grants No. A2021202002 and No. A2021202012), the Overseas Scientists Sponsorship Program of Hebei Province (Grant No. C20210330), Guangdong Foundation for Basic and Applied Basic Research-Joint Foundation of Dongguan-Guangdong Province (Grant No. 2020A1515111109), the National Natural Science Foundation of China (Grant No. 12004096), the "State Key Laboratory of Reliability and Intelligence of Electrical Equipment" of Hebei University of Technology (Grant No. EERI-PI2020009), and the Doctoral Postgraduate Innovation Funding project of Hebei Province (Grant No. CXZZBS2021028).

[1] P. B. Pal, Am. J. Phys. **79**, 485 (2011).
[2] N. P. Armitage, E. J. Mele, and A. Vishwanath, Rev. Mod. Phys. **90**, 015001 (2018).
[3] S. A. Yang, SPIN **06**, 1640003 (2016).
[4] X. Wan, A. M. Turner, A. Vishwanath, and S. Y. Savrasov, Phys. Rev. B **83**, 205101 (2011).
[5] S.-Y. Xu, I. Belopolski, N. Alidoust, M. Neupane, G. Bian, C. Zhang, R. Sankar, G. Chang, Z. Yuan, C.-C. Lee, S.-M. Huang, H. Zheng, J. Ma, D. S. Sanchez, B. Wang, A. Bansil, F. Chou, P. P. Shibayev, H. Lin, S. Jia *et al.*, Science **349**, 613 (2015).
[6] L. Lu, Z. Wang, D. Ye, L. Ran, L. Fu, J. D. Joannopoulos, and M. Soljačić, Science **349**, 622 (2015).
[7] S. M. Young, S. Zaheer, J. C. Y. Teo, C. L. Kane, E. J. Mele, and A. M. Rappe, Phys. Rev. Lett. **108**, 140405 (2012).
[8] B.-J. Yang and N. Nagaosa, Nat. Commun. **5**, 4898 (2014).
[9] B.-J. Yang, T. Morimoto, and A. Furusaki, Phys. Rev. B **92**, 165120 (2015).
[10] Z. Gao, M. Hua, H. Zhang, and X. Zhang, Phys. Rev. B **93**, 205109 (2016).
[11] B.-J. Yang, T. A. Bojesen, T. Morimoto, and A. Furusaki, Phys. Rev. B **95**, 075135 (2017).
[12] W. Wu, Z.-M. Yu, X. Zhou, Y. Zhao, and S. A. Yang, Phys. Rev. B **101**, 205134 (2020).
[13] L. Jin, X. Zhang, Y. Liu, X. Dai, L. Wang, and G. Liu, Phys. Rev. B **102**, 195104 (2020).
[14] B. Bradlyn, J. Cano, Z. Wang, M. Vergniory, C. Felser, R. Cava, and B. Bernevig, Science **353**, 558 (2016).
[15] Z. Zhu, G. W. Winkler, Q. Wu, J. Li, and A. A. Soluyanov, Phys. Rev. X **6**, 031003 (2016).
[16] L. Tian, Y. Liu, W.-W. Yu, X. Zhang, and G. Liu, Phys. Rev. B **104**, 045137 (2021).
[17] X. Feng, W. Wu, Z.-M. Wu, and S. A. Yang, Phys. Rev. B **104**, 115116 (2021).
[18] L. Jin, X. Zhang, X. Dai, H. Liu, G. Chen, and G. Liu, J. Mater. Chem. C **7**, 1316 (2019).
[19] S. Nie, B. A. Bernevig, and Z. Wang, Phys. Rev. Research **3**, L012028 (2021).
[20] L. Jin, Y. Liu, X. Zhang, X. Dai, and G. Liu, Phys. Rev. B **104**, 045111 (2021).
[21] L. Tian, Y. Liu, W. Meng, X. Zhang, X. Dai, and G. Liu, J. Phys. Chem. Lett. **11**, 10340 (2020).
[22] Z. P. Sun, C. Q. Hua, X. L. Liu, Z. T. Liu, M. Ye, S. Qiao, Z. H. Liu, J. S. Liu, Y. F. Guo, Y. H. Lu, and D. W. Shen, Phys. Rev. B **101**, 155114 (2020).
[23] X. Yáng, T. A. Cochran, R. Chapai, D. Tristant, J.-X. Yin, I. Belopolski, Z. Chéng, D. Multer, S. S. Zhang, N. Shumiya, M. Litskevich, Y. Jiang, G. Chang, Q. Zhang, I. Vekhter, W. A. Shelton, R. Jin, S.-Y. Xu, and M. Z. Hasan, Phys. Rev. B **101**, 201105(R) (2020).
[24] N. B. Schröter, D. Pei, M. G. Vergniory, Y. Sun, K. Manna, F. De Juan, J. A. Krieger, V. Süss, M. Schmidt, P. Dudin *et al.*, Nat. Phys. **15**, 759 (2019).
[25] P. Tang, Q. Zhou, and S.-C. Zhang, Phys. Rev. Lett. **119**, 206402 (2017).
[26] D. Takane, Z. Wang, S. Souma, K. Nakayama, T. Nakamura, H. Oinuma, Y. Nakata, H. Iwasawa, C. Cacho, T. Kim, K. Horiba, H. Kumigashira, T. Takahashi, Y. Ando, T. Sato, Phys. Rev. Lett. **122**, 076402 (2019).
[27] B. Lv, Z.-L. Feng, J.-Z. Zhao, N. F. Yuan, A. Zong, K. Luo, R. Yu, Y.-B. Huang, V. Strocov, A. Chikina, A. A. Soluyanov, N. Gedik, Y. G. Shi, T. Qian, H. Ding, Phys. Rev. B **99**, 241104(R) (2019).
[28] S. Thirupathaiah, Y. Kushnirenko, K. Koepernik, B. R. Piening, B. Büchner, S. Aswartham, J. van den Brink, S. Borisenko, and I. C. Fulga, SciPost Phys. **10**, 004 (2021).
[29] G. Chang, S.-Y. Xu, B. J. Wieder, D. S. Sanchez, S.-M. Huang, I. Belopolski, T.-R. Chang, S. Zhang, A. Bansil, H. Lin *et al.*, Phys. Rev. Lett. **119**, 206401 (2017).
[30] X. Zhang, Q. Gu, H. Sun, T. Luo, Y. Liu, Y. Chen, Z. Shao, Z. Zhang, S. Li, Y. Sun, Y. Li, X. Li, S. Xue, J. Ge, Y. Xing, R. Comin, Z. Zhu, P. Gao, B. Yan, J. Feng *et al.*, Phys. Rev. B **102**, 035125 (2020).
[31] L. Wang, X. Zhang, W. Meng, Y. Liu, X. Dai, and G. Liu, J. Mater. Chem. A **9**, 22453 (2021).
[32] S. Han, C. Lee, E.-G. Moon, and H. Min, Phys. Rev. Lett. **122**, 187601 (2019).
[33] J.-R. Wang, G.-Z. Liu, and C.-J. Zhang, Phys. Rev. B **99**, 195119 (2019).
[34] S.-X. Zhang, S.-K. Jian, and H. Yao, Phys. Rev. B **103**, 165129 (2021).
[35] Q. Chen and G. A. Fiete, Phys. Rev. B **93**, 155125 (2016).
[36] H.-F. Zhu, X.-Q. Yang, J. Xu, and S. Cao, Eur. Phys. J. B **93**, 4 (2020).

[37] F. Flicker, F. de Juan, B. Bradlyn, T. Morimoto, M. G. Vergniory, and A. G. Grushin, Phys. Rev. B **98**, 155145 (2018).
[38] W. Meng, X. Zhang, Y. Liu, X. Dai, G. Liu, and L. Kou, arXiv:2104.03478 (2021)
[39] Z.-M. Yu, Z. Zhang, G.-B. Liu, W. Wu, X.-P. Li, R.-W. Zhang, S. A. Yang, and Y. Yao, Sci. Bull. **67**, 375 (2022).
[40] N. Kumar, M. Yao, J. Nayak, M. G. Vergniory, J. Bannies, Z. Wang, N. B. M. Schröter, V. N. Strocov, L. Müchler, W. Shi, E. D. L. Rienks, J. L. Mañes, C. Shekhar, S. S. P. Parkin, J. Fink, G. H. Fecher, Y. Sun, B. A. Bernevig, and C. Felser, Adv. Mater. **32**, 1906046 (2020).
[41] F. Hulliger, Mater. Res. Bull. **14**, 33 (1979).
[42] J. Alonso, J. Boucherle, J. Rossat-Mignod, J. Schweizer, T. Suzuki, and T. Kasuya, J. Magn. Magn. Mater. **103**, 179 (1992).
[43] T. Suzuki, O. Nakamura, N. Tomonaga, S. Ozeki, Y. Kwon, A. Ochiai, T. Takeda, and T. Kasuya, Phys. B: Condens. Matter **163**, 131 (1990).
[44] F. Holtzberg, T. McGuire, S. Methfessel, and J. Suits, J. Appl. Phys. **35**, 1033 (1964).
[45] H. Kang, D. Kim, J. Kim, G. McIntosch, Y. Park, K. Nahm, and J. Pelzl, Physica C: Supercond. Applic. **364**, 329 (2001).
[46] A. T. Starovoitov, V. I. Ozhogin, G. Loginov, and V. Sergeeva, Zh. Eksp. Teor. Fiz. **57**, 791 (1969).
[47] O. Massenet, J. Coey, and F. Holtzberg, Le J. Phys. Colloq. **37**, C4-297 (1976).
[48] K. Yaguchi, J. Phys. Soc. Jpn. **22**, 673 (1967).
[49] G. Amoretti, M. Bogé, J. Fournier, A. Blaise, and A. Wojakowski, J. Magn. Magn. Mater. **66**, 236 (1987).
[50] P. Burlet, J. Rossat-Mignod, R. Troć, and Z. Henkie, Solid State Commun. **39**, 745 (1981).
[51] A. Gukasov, P. Wiśniewski, and Z. Henkie, Phys. B: Condens. Matter **234**, 694 (1997).
[52] W. Suski, T. Mydlarz, and V. Rao, Phys. Stat. Sol. (a) **14**, K157 (1972).
[53] B. Dunlap, D. Lam, G. Kalvius, and G. Shenoy, J. Appl. Phys. **42**, 1719 (1971).
[54] T. Herrmannsdörfer, P. Fischer, P. Wachter, G. Wetzel, and K. Mattenberger, Solid State Commun. **112**, 135 (1999).
[55] S. Sportouch and M. G. Kanatzidis, J. Solid State Chem. **162**, 158 (2001).
[56] T. Ohama, H. Yasuoka, T. Takabatake, and H. Fujii, Phys. B: Condens. Matter **186**, 717 (1993).
[57] G. Kresse and D. Joubert, Phys. Rev. B **59**, 1758 (1999).
[58] P. E. Blöchl, Phys. Rev. B **50**, 17953 (1994).
[59] J. P. Perdew, K. Burke, and M. Ernzerhof, Phys. Rev. Lett. **77**, 3865 (1996).
[60] N. Marzari and D. Vanderbilt, Phys. Rev. B **56**, 12847 (1997).
[61] A. A. Mostofi, J. R. Yates, Y.-S. Lee, I. Souza, D. Vanderbilt, and N. Marzari, Comput. Phys. Commun. **178**, 685 (2008).
[62] Q. Wu, S. Zhang, H.-F. Song, M. Troyer, and A. A. Soluyanov, Comput. Phys. Commun. **224**, 405 (2018).
[63] M. Jansen and N. Korber, Z. Anorg. Allg. Chem. **598**, 163 (1991).
[64] J. J. Attema, G. A. de Wijs, G. R. Blake, and R. A. de Groot, J. Am. Chem. Soc. **127**, 16325 (2005).
[65] E. V. Gorbar, V. A. Miransky, I. A. Shovkovy, and P. O. Sukhachov, Phys. Rev. B **91**, 121101(R) (2015).
[66] S.-Y. Xu, C. Liu, S. K. Kushwaha, R. Sankar, J. W. Krizan, I. Belopolski, M. Neupane, G. Bian, N. Alidoust, T.-R. Chang *et al.*, Science **347**, 294 (2015).
[67] M. Neupane, S.-Y. Xu, R. Sankar, N. Alidoust, G. Bian, C. Liu, I. Belopolski, T.-R. Chang, H.-T. Jeng, H. Lin *et al.*, Nat. Commun. **5**, 3786 (2014).
[68] Z. Wang, H. Weng, Q. Wu, X. Dai, and Z. Fang, Phys. Rev. B **88**, 125427 (2013).
[69] H. Yi, Z. Wang, C. Chen, Y. Shi, Y. Feng, A. Liang, Z. Xie, S. He, J. He, Y. Peng *et al.*, Sci. Rep. **4**, 6106 (2014).
[70] M. Kargarian, M. Randeria, and Y.-M. Lu, Proc. Natl. Acad. Sci. USA **113**, 8648 (2016).
[71] C. Fang, M. J. Gilbert, X. Dai, and B. A. Bernevig, Phys. Rev. Lett. **108**, 266802 (2012).